# Effect of Main Blade Configuration on the Performance of the Optimized Multicurve Savonius Wind Turbine

Banh Duc Minh[1], Le Dinh Anh[1(✉)], Tran Cuong Hung[2], Doan Viet Ha[3], Tran Cong Manh Hung[3], and Nguyen Thi Thu Phuong[3]

[1] School of Aerospace Engineering, VNU-University of Engineering and Technology, Vietnam National University, Hanoi, Vietnam
`anh.ld@vnu.edu.vn`
[2] Faculty of Engineering Mechanics and Automation, VNU-University of Engineering and Technology, Vietnam National University, Hanoi, Vietnam
[3] VNU-University of Engineering and Technology, Vietnam National University, Hanoi, Vietnam

**Abstract.** This study numerically investigates the effect of multi-curve blade configuration on the performance of the optimized Savonius wind turbine. The simulation is performed utilizing a sequence of unsteady 2D computational fluid dynamics in the commercial software ANSYS Fluent 2021R2. The results state a high influence of the turbine performance on the multi-curve shape. The highest performance of the rotor is recognized on the blade configuration with the main profile made by a quarter circular $R_3{}^* = 0.5$ and a quarter elliptical section. For which, the power coefficient $C_p$ is improved by 185.1% at the tip speed ratio (TSR) higher than 1.0 and up to 5.5% at TSR of less than 0.8, making this design better suited for wide working conditions over the previous configurations.

**Keywords:** Savonius · Renewable energy · Multi-curve blade · Realizable $k$-$\varepsilon$ · Tip speed ratio

## 1 Introduction

Savonius wind turbine, built by engineer S. J. Savonius [1, 2], is a popular vertical axis wind turbine (VAWT) used in both urban and rural areas. The advanced features of the Savonius turbine include simple assembly, low maintenance costs, low starting speed, omnidirectional operation, and low noise. However, the efficiency of the Savonius turbine is still relatively low compared to other turbines.

Many studies have been carried out to improve the efficiency of Savonius turbines including flow control by flow deflectors [3, 4] and improved blade profiles [5–13]. With flow deflectors, the wind will be oriented to the advancing blade and blocked from the returning blade. However, in this technique, the advanced features of the Savonius turbine were eliminated such as its compactness size and the independence of wind direction. Therefore, at the present, most of the research focuses on the optimizing blade shape such

as an overlap blade type [5], a modified blade with variable thickness [6, 7], Bach-type [8–10], elliptical and multi-curve type [11, 12], and multi-blade [13]. Compared with the conventional turbine, the power coefficient $C_p$ of the Savonius rotor can be improved up to hundreds of percent depending on the blade configuration [11]. However, previous blade designs were only paid attention to specific operating conditions such as the low TSR range of lower than 0.8 for rural application or high TSR > 1.2 for use in urban environments.

In this study, various blade configurations for the Savonius rotor are investigated to recognize the best configuration with the highest performance in wide operating ranges. The multi-curve blade is designed, for which the main profile is made by a quarter circle with a non-dimensional radius $R_3{}^*$ and a quarter elliptical section. The performance of the optimized design and its advantage against the conventional one are analyzed utilizing a sequence unsteady simulation in commercial software ANSYS Fluent 2021R2.

## 2 Geometry Design for Optimized Rotors with R3* Varies

Based on flow characteristics around the blade, and from previous research on the elliptical and multi-curve blade [11], the new multi-curve blade is designed. Figure 1 illustrates a configuration of the conventional blade OB [14] (a) and the designed multi-curve blade shapes in this study according to the non-dimensional radius of the quarter circular profile $R_3{}^*$. Here, the optimized blade is named MB02 to MB06 which is proportional to the $R_3{}^*$ ranging from 0.2 to 0.6, respectively. The detailed designed parameters for conventional and optimized blade configurations are presented in Table 1.

## 3 Numerical Simulation

### 3.1 Numerical Method

In this study, the flow around the rotor blade is numerically analyzed utilizing the sequence unsteady simulation, which is performed using the commercial Computational Fluid Dynamics software ANSYS Fluent 2021R2. For which, the governing equation for a 2D incompressible unsteady Reynolds-Averaged Navier-Stokes equation is derived as follows [11]:

$$\frac{\partial \overline{u}_i}{\partial x_i} = 0 \tag{1}$$

$$\frac{\partial \overline{u}_i}{\partial t} + \frac{\partial}{\partial x_j}\left(\overline{u}_i \overline{u}_j\right) = \frac{-1}{\rho}\frac{\partial \overline{p}}{\partial x_i} + \frac{\partial}{\partial x_j}\left(v\frac{\partial \overline{u}_i}{\partial x_j} - \overline{u}_i \overline{u}_j\right) \tag{2}$$

Here, $\overline{p}$, $\overline{u}$, $u'$, and $v$ are the pressure, the mean velocity, the fluctuation velocity, and the kinematic viscosity of the wind flow, respectively. $u_i' u_j'$ denoted the Reynolds stress tensor. The realizable $k$-$\varepsilon$ turbulence model and the enhanced wall function are selected to account for the effect of the turbulence on the flow around the rotor [11].

The implicit pressure-based solver with the coupled method was used to solve the governing equation above. The second-order upwind method was applied for the discretization of the convection equations. The least-square cell-based method was used for the gradient. Besides, the second-order implicit method is used for the time variable. The rotation of the rotor is simulated using the sliding mesh model.
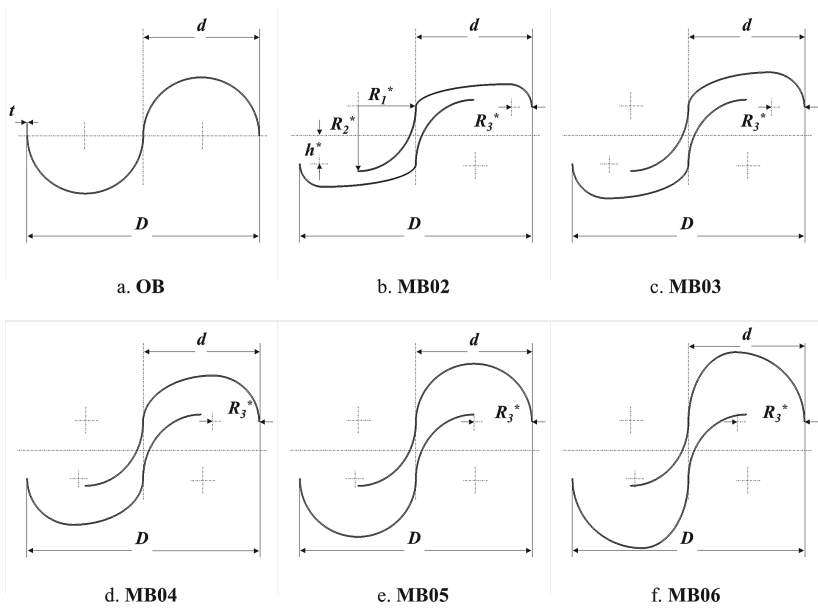
**Fig. 1.** Geometry and parameters of blade configurations (a–f)

**Table 1.** Details of rotor configuration design parameters [m]

|        | $d$ [m] | $D$ [m] | $t$ [m] | $h*$  | $R_1*$ | $R_2*$ | $R_3{}^*$ |
|--------|---------|---------|---------|-------|--------|--------|-----------|
| MB02   | 0.5     | 1       | 0.004   | 0.25  | 0.5    | 0.55   | 0.2       |
| MB03   |         |         |         |       |        |        | 0.3       |
| MB04   |         |         |         |       |        |        | 0.4       |
| MB05   |         |         |         |       |        |        | 0.5       |
| MB06   |         |         |         |       |        |        | 0.6       |
| OB     | 0.5     | 1       | 0.004   | –     | –      | –      | –         |

## 3.2   Computational Domain and Simulation Conditions

Figure 2 illustrates the computational domain, boundary conditions, and mesh details used for the simulation. The domain includes a rotating zone of size 1.2$D$ placed at a distance of 6$D$ and 10$D$ from the inlet and outlet boundaries, respectively. The stationary zone has a size of 16$D$ × 14$D$ with two side boundaries located symmetry from the rotor center. These two zones are connected by an interface model.

At the inlet boundary, the wind velocity $U_0 = 7$ m/s [14], and the turbulent quantities are specified [11, 13]. The symmetry condition is applied at the two-side boundaries, meanwhile, the no-slip condition is used for the rotor blade. Depending on the specific TSR, the rotating zone has different rotational speeds $\omega$, as shown in Table 2. The rotation

of $2^0$/step is set for the time step size. And the simulation is performed for the completion of 10 rotations.

The unstructured mesh is generated over the domain. Regarding the mesh indepen-dency study, the mesh is generally fine at the rotor-stator interface with the minimum size of 0.005m and at the blade shape with the minimum size of 0.001 m. The coarse mesh is used for the stationary zone. Near the blade surface, the structured mesh with 20 layers, in which the first layer thickness is $10^{-5}$ corresponding to mesh resolution of $y^+ < 1$, is generated.
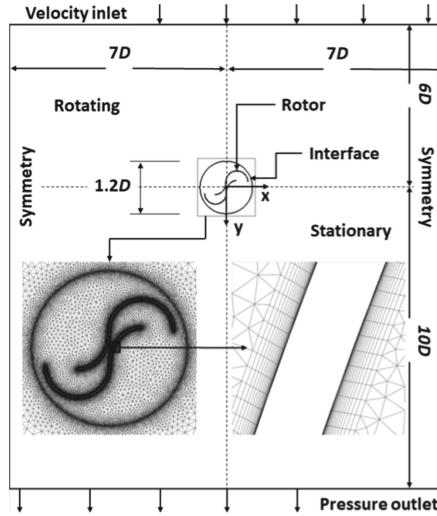


**Fig. 2.** Computational domain, boundary conditions and mesh detail around rotor

**Table 2.** Rotational speed of rotating zone, $\omega$ [rad/s]

| $\lambda$ | 0.67 | 0.8 | 0.9 | 1.0 | 1.1 | 1.2 | 1.3 | 1.4 | 1.5 | 1.6 |
|---|---|---|---|---|---|---|---|---|---|---|
| $\omega$ | 9.38 | 11.2 | 12.6 | 14 | 15.4 | 16.8 | 16.8 | 19.6 | 21 | 22.4 |

## 4  Results and Discussions

### 4.1  Torque Distribution in One Period Rotating

Figure 3 illustrates the comparison of the averaged moment $C_m$ and power $C_p$ coefficients between the conventional and the optimized blade configurations with different $R_3{}^*$ at various TSRs. For which, $C_m$ decreases as TSR gradually increases. Rotor MB02 has the lowest $C_m$ of configurations considered in all TSRs. Meanwhile, at TSR > 1.0, rotors MB04, MB05, and MB06 perform significantly better than the other rotor. $C_m$ decreases

slowly with a gentler slope at TSR between 1.0 and 1.4 in these 3 rotors. Although the optimized MB04 rotor has a lower $C_p$ than the previously studied MB05 rotor [11] at TSR from 1.0 to 1.4, this rotor allows more efficient operation in wider wind conditions. Specifically, the MB04 rotor gives greater efficiency at TSRs < 1.0 and TSRs > 1.4. The best performance that the MB04 rotor offers improves up to 5.5% at TSR < 1.0 and up to 185.1% at TSR > 1.4 when compared to the OB rotor. This greatly increases the energy efficiency that this turbine produces at both low TSRs and high TSRs, thereby demonstrating the applicability of the rotor MB04 under wider operating conditions than in previous studies.
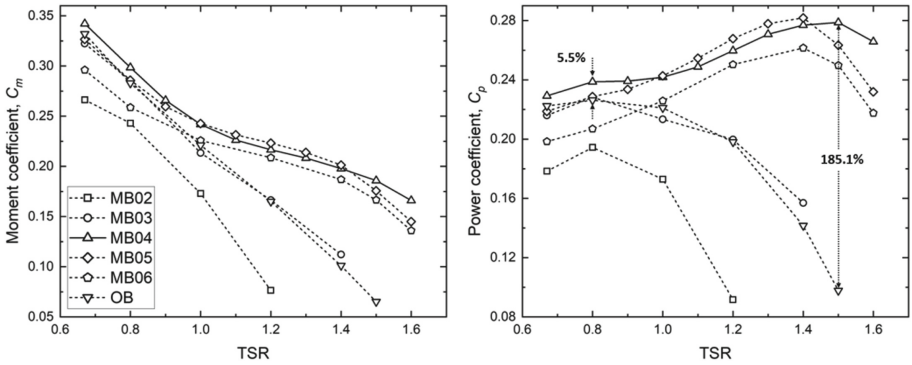


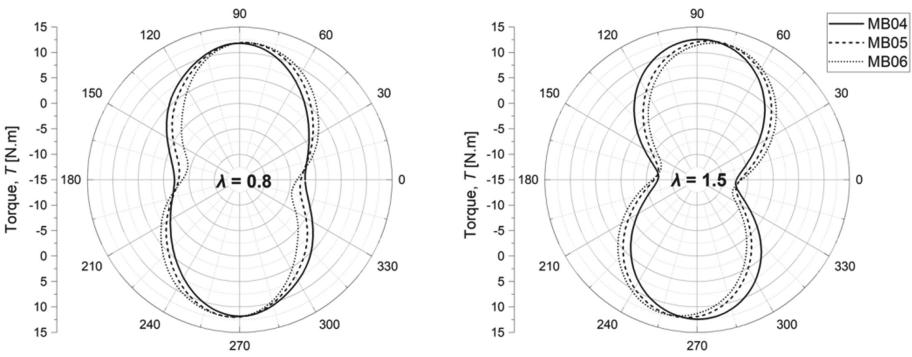**Fig. 3.** Averaged $C_p$ and $C_m$ with $R_3{}^*$ varied



**Fig. 4.** Torque distribution in one period rotating

Figure 4 presents the distribution of torque in one rotation at TSR 0.8 and 1.5 between the rotor with blades MB04, MB05, and MB06. At TSR 0.8, the rotor with blade MB04 produces a higher torque area than that with blades MB05 and MB06 at azimuths from 80° to 175° and from 260° to 355°. Similar behavior can be seen at TSR = 1.5. For which the area with the higher torque in the rotor with blade MB04 is much larger than the area with the higher torque in the rotor with blades MB05 and MB06, responding to better performance on the MB04 rotor, as shown in Fig. 3.

## 5   Conclusion

In this study, a multi-curve blade configuration that improves the performance of a Savonius rotor is numerically recognized. The advanced feature of the optimized design against the conventional one is analyzed through a sequence unsteady simulation using the commercial CFD software Ansys Fluent 2021R2.

The results suppose a high dependency of the rotor performance on the main blade configuration. The best performance is observed with blade MB04 with $R_3{}^* = 0.4$ with the increment in power coefficient by 185% at high TSR of greater than 1.0 and up to 5.5% at low TSR range of less than 0.8 over the other configurations. The result implies a high potential application of the rotor with blade MB04 for energy harvesting application in wide wind conditions.

## References

1. Joselin Herbert, G.M., Iniyan, S., Sreevalsan, E., Rajapndian, S.: A review of wind energy technology. Renew. Sustain. Energy. Rev. **11**(6), 1117–45 (2007)
2. Savonius, S.J.: The S-rotor and its application. Mech. Eng. **53**, 333–8 (1931)
3. Mohamed, M.H., Thevenin, D.: Performance optimization of a Savonius turbine considering different shapes for frontal guiding plates. In: 10th International Congress of Fluid Dynamics, Stella Di Mare Sea Club Hotel, Ain Soukhna, Red Sea, Egypt (2010)
4. El-Askary, W.A., Nasef, M.H., Abdel-Hamid, A.A., Gad, H.E.: Harvesting wind energy for improving performance of Savonius rotor, J. Wind Eng. Ind. Appl. **139**, 8–15 (2015)
5. Al-Faruk, A., Sharifian, A.: Blade overlap and blade angle on the aerodynamic coefficients in vertical axis swirling type Savonius wind turbine. In: 19th Australasian Fluid Mechanics Conference, Melbourne, Australia (2014)
6. Saeed, H.A.H., Elmekawy, A.M.N., Kassab, S.Z.: Numerical study of improving Savonius turbine power coefficient by various blade shapes. Alex. Eng. J. **58**, 429–441 (2019)
7. Kollmann, T.: J. In: Kollmann, T., Kuckertz, A., Stöckmann, C. (eds.) Gabler Kompakt-Lexikon Unternehmensgründung, pp. 223–224. Springer, Wiesbaden (2021). https://doi.org/10.1007/978-3-658-30901-5_10
8. Kamoji, M.A., Kedare, S.B., Prabhu, S.V.: Experimental investigations on modified Savonius rotor. Appl. Energy **86**(7–8), 1064–1073 (2009)
9. Kacprzak, K., Liskiewicz, G., Sobczak, K.: Numerical investigation of conventional and modified Savonius wind turbines. Renew. Energy **60**, 578–585 (2013)
10. Roy, S., Saha, U.K.: Wind tunnel experiments of a newly developed two-bladed Savonius-style wind turbine. Appl. Energy **137**, 117–125 (2015)
11. Anh, D.L., Minh, B.D., Tam, H.V., Hung, T.T.: Modified Savonius wind turbine for wind energy harvesting in urban environments, ASME. J. Fluids Eng. **144**(8), 081501 (2022)
12. Anh, D.L., Minh, B.D., Trinh, C.D.: High efficiency energy harvesting using a Savonius turbine with multicurve and auxiliary blade, ASME. J. Fluids Eng. **144**(11), 111207 (2022)
13. Hassanzadeh, R., Mohammadnejad, M., Mostafavi, S.: Comparison of various blade profiles in a two-blade conventional Savonius wind turbine, ASME. J. Energy Resour. Technol **143**(2), 021301 (2021)
14. Blackwell, B.F., Sheldahl, R.E., Feltz, L.V.: Wind tunnel performance data for two and three-bucket Savonius rotors, SAND76-01321 UC-60, National Tech. Information Service, U. S. Dept. Commerce, Springfield, VA 22161 (1977)